Excited-state absorption spectra of V^{2+} in $KMgF_3$ and MgF_2

Stephen A. Payne, L. L. Chase, and Gary D. Wilke
Lawrence Livermore National Laboratory, University of California, P.O. Box 5508, Livermore, California 94550
(Received 8 September 1987)

We have measured the excited-state absorption spectra of V^{2+} in $KMgF_3$ and MgF_2. The observed absorption bands can be identified as being due to the ${}^4T_2 \rightarrow {}^4T_1 a$ and ${}^4T_1 b$ transitions. The position and shape of the ${}^4T_2 \rightarrow {}^4T_1 b$ transition are determined primarily by the displacement in the a_{1g} mode while the coupling of the orbital triplet states to e_g distortions is found to have a substantial influence on the nature of the ${}^4T_2 \rightarrow {}^4T_1 a$ transition. In fact, this transition is observed as a broad band rather than as a sharp line, as is predicted solely on the basis of the a_{1g} coordinate. The ${}^4T_2 \rightarrow {}^4T_1 a$ transition is shifted up in energy relative to its predicted position and significantly overlaps the emission spectrum, thereby providing an explanation for the poor lasing efficiency reported for V^{2+} lasers.

I. INTRODUCTION

The $MgF_2:V^{2+}$ laser was first discovered by Johnson, Guggenheim, and Thomas in 1966.[1] This material was then reexamined in detail by Krupke in 1980 for the potential application as a fusion laser medium.[2] The performance of the V^{2+}-impurity laser needed to be quantitatively assessed, and in several subsequent reports Moulton, Fahey, and Krupke showed that the stimulated emission cross sections of V^{2+} in MgF_2 and $KMgF_3$ were far less than the values predicted on the basis of the emission spectra and lifetime.[3,4] The detriment in gain was attributed to excited-state absorption (ESA) primarily because the authors found no indication that the poor laser performance was due to nonradiative decay or to passive optical losses. These disappointing results indicated that, while V^{2+} does exhibit gain, it could not be expected to operate efficiently as a laser. Brauch and Dürr recently lased $CsCaF_3:V^{2+}$ and also found a low slope efficiency, although they were uncertain as to its origin.[5,6]

In this work, we have directly measured the ESA by means of a pump-probe experiment. The motivation for this effort was to develop a physical understanding of the origin of the ESA bands, thereby providing new insights into the impurity-lattice interactions of the V^{2+} ion. These results also have direct bearing on the laser properties of the isoelectronic ion Cr^{3+} in many hosts.

Sturge and co-workers have previously determined the optical spectra and energy levels of V^{2+} in $KMgF_3$ and MgF_2.[7] The spectral observations are well explained with reference to the d^3 Tanabe-Sugano diagram for octahedral coordination.[8] Within the strong-field description, we may consider the $3d$ orbital as being split into two groups: three t_2 orbitals lying $4Dq$ below the baricenter, and two e orbitals $6Dq$ above. The ground state arises from the occupation of the t_2 orbitals at the maximum spin multiplicity, and is therefore designated by ${}^4A_2(t_2^3)$. Three additional excited state quartets are derived from the $t_2^2 e$ and $t_2 e^2$ configurations; they are the ${}^4T_2(t_2^2 e)$, ${}^4T_1 a(t_2^2 e)$, and ${}^4T_1 b(t_2 e^2)$ states. Three spin-allowed absorptions, due to the ${}^4A_2 \rightarrow {}^4T_2$, ${}^4T_1 a$, and ${}^4T_1 b$ transitions, are observed as broad bands, while the ${}^4T_2$ excited state is found to be metastable and to emit via the ${}^4T_2 \rightarrow {}^4A_2$ transition.

The possibility of ESA also exists; it would be expected to arise from the ${}^4T_2 \rightarrow {}^4T_1 a$ and ${}^4T_1 b$ transitions. As a general rule of thumb, it has often been thought that transitions involving different d-electron configurations are observed to be broad, while those involving a single electronic configuration would be sharp. These simple predictions have been found to be in agreement with the ground-state absorption spectra. The ${}^4A_2(t_2^3) \rightarrow {}^4T_2(t_2^2 e)$, ${}^4T_1 a(t_2^2 e)$, and ${}^4T_1 b(t_2 e^2)$ transitions are observed as broad bands, while the ${}^4A_2(t_2^3) \rightarrow {}^2E(t_2^3)$, ${}^2T_1(t_2^3)$, and ${}^2T_2(t_2^3)$ transitions are seen as sharp features. Using these same arguments we might expect the ${}^4T_2(t_2^2 e) \rightarrow {}^4T_1 a(t_2^2 e)$ ESA band to be sharp and the ${}^4T_2(t_2^2 e) \rightarrow {}^4T_1 b(t_2 e^2)$ transition to be observed as a broad band. We will show in this paper, however, that these simple arguments appear to be only partly justified for the ESA spectra of the V^{2+} impurity.

II. EXPERIMENT

The excited-state absorption spectra of the V^{2+} impurity were measured using a classic pump-probe experimental arrangement, in which the transmission of a probe beam is compared in the presence and absence of a pump pulse. If the light intensity incident on the sample is I_0 and the transmitted intensity of the unpumped sample is I_u, we define the optical absorption of the unpumped sample to be

$$-\ln(I_u/I_0) = \sigma_g N l \ , \tag{1}$$

where σ_g is the ground-state cross section, N is the total V^{2+} concentration, and l is the sample length. The absorption in the presence of the pump laser is

$$-\ln(I_p/I_0)=\int_0^l \sigma_g[N-N_p(l)]dl+\int_0^l \sigma_e N_p(l)dl \ , \tag{2}$$

where $N_p(l)$ is the nonuniform distribution of excited V^{2+} ions created by the pump source, and σ_e is the excited-state absorption cross section. If we assume that the changes in the probe beam are small, the resulting difference spectrum is

$$A_d=(I_u-I_p)/I_u \ . \tag{3}$$

Thus we find that

$$A_d=(\sigma_e-\sigma_g)\int_0^l N_p(l)dl \ . \tag{4}$$

From Eqs. (3) and (4) we see that excited-state absorption bands will be observed as positive features while the ground-state bleaching signal will be negative.

In practice, the fluorescence background as well as the effects of electronic noise must be taken into account in order to accurately determine the value of A_d. To do this, a cycle consisting of four measurements is required and Eq. (3) is modified to be

$$A_d=\frac{[I(\text{probe only})-I(\text{neither})]-[I(\text{pump+probe})-I(\text{pump only})]}{[I(\text{probe only})-I(\text{neither})]} \ . \tag{5}$$

The experimental arrangements illustrated in Fig. 1 were used to obtain data in the ultraviolet, visible, and infrared spectral regions. The two setups involve the use of different detectors and sources of light, but the theory of the measurement is based on Eq. (5) for both cases.

In order to obtain the ESA data in the visible region, the setup schematically shown in Fig. 1(a) was used. A cw tungsten-halogen lamp was focused through a pinhole to provide a suitable image to be refocused onto the sample. The yttrium-aluminum-garnet (YAG) laser was frequency-converted to the third harmonic at 355 nm, and was focused onto the same sample volume as the probe beam. The two beams are collinearly arranged by using an appropriate dichroic mirror. The probe beam was then directed into a polychromator which imaged the spectrum onto a reticon array detector (EG&G PAR1420), so that the entire spectrum was accumulated each time the reticon was read. A clock triggered the reticon reading cycle at 20 Hz, while the reticon controller (OMA III) sent a trigger pulse to the laser prior to every other reading of the detector. The reticon was gated using the high-voltage pulse generator, such that the intensifier was switched on only during the excited-state lifetime of the V^{2+} ions. Using this arrangement, the values of I(probe only) and I(pump+probe) from Eq. (5) were determined. I(neither) and I(pump only) were measured by using the same experimental procedure and simply blocking the probe beam. The software provided by PAR was used to calculate the difference spectra and smooth the data. The ESA spectra in the ultraviolet region were obtained by operating the laser at the second harmonic (532 nm), changing the dichroic mirror in the probe beam path, and using a cw xenon lamp as the probe source.

The experimental arrangement depicted in Fig. 1(b) was used to obtain ESA data in the infrared spectral region. Note that the optical arrangement is similar to that of Fig. 1(a). The differences involve the use of a flashlamp-pumped dye laser (Candela, model LFDL-6SG) and an InSb infrared detector (Santa Barbara, model 9209). This setup requires that the monochromator be scanned; this and other interfacing requirements were satisfied with the aid of a Digital Equipment Corporation LSI-11 computer. The computer served as the clock for these experiments, the dye laser being triggered at half the rate at which the InSb detector output was

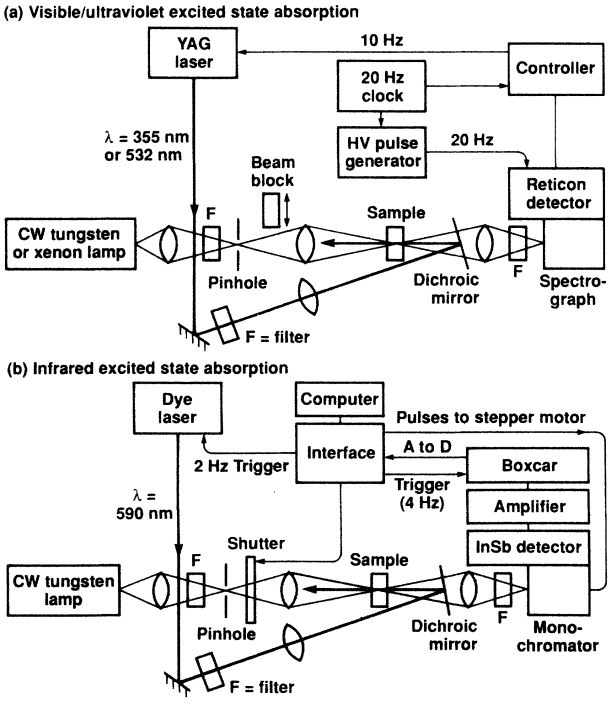

FIG. 1. Pump-probe experimental setups used to measure the excited-state absorption spectra of the V^{2+} impurity in the indicated spectral regions. Arrangements (a) and (b) are similar in that they involve the collinear propagation of the pump and probe beams through the sample, the use of a cw probe source, and gated detection. They differ in the selection of the pump source, and the use of single wavelength detection in (b) vs multiplexed spectral acquisition in (a).

measured (4 Hz). The boxcar gate was adjusted to measure the light level only during the lifetime of the excited V^{2+} ions. The computer also operated a shutter to block the probe beam such that all the quantities represented in Eq. (5) could be measured.

It is interesting to compare the relative utility of the two experiments represented in Fig. 1. The setup in Fig. 1(a) has the advantages of a higher repetition rate and multiplexed spectral acquisition. The main disadvantage arises from the short pulse width of the pump laser. Since the V^{2+} excited-state lifetime is on the order of a millisecond, the YAG laser pulse width of several nanoseconds is unnecessarily short. The result is that the maximum laser energy which may impinge upon the sample is limited by the surface damage threshold. On the other hand, the setup shown in Fig. 1(b) involves the use of a flashlamp-pumped dye laser that has a 1-μs pulse width, thereby allowing the use of greater pump energy. The net result was that the probe beam changes were on the order of 0.03% and 3% for the use of the YAG laser versus the dye laser, respectively. From our experiences, we found that the disadvantages of the lower repetition rate and the single wavelength detection were easily offset by the allowable use of greater pump energy. In fact, spectra of comparable quality required 10 h of accumulation for the arrangement shown in Fig. 1(a), compared with only 1 h for that of Fig. 1(b).

III. RESULTS

We have obtained the excited-state absorption (ESA) spectra of V^{2+} in $KMgF_3$ and MgF_2. These materials were selected in part because they have been well characterized by conventional spectroscopic methods. In addition, their stimulated emission cross sections have been previously measured, thereby providing an indirect assessment of the ESA cross sections with which we can compare the present results. Now, the Mg^{2+} site in $KMgF_3$ is rigorously octahedral, while a tetragonal distortion exists in the case of the MgF_2 host, resulting in substantial splittings in the observed spectra. For this reason, in what follows, we will primarily analyze the simpler $KMgF_3:V^{2+}$ system, and regard the data on $MgF_2:V^{2+}$ simply as supportive evidence.

A. $KMgF_3:V^{2+}$

The ground- and excited-state spectra of $KMgF_3:V^{2+}$ are displayed in Fig. 2. The conventional absorption and emission spectra are shown in the lower frame. The absolute values of the cross sections were taken from Refs. 9 and 4. The three broad bands arise from the $^4A_2 \rightarrow {}^4T_2$, ^4T_1a, and ^4T_1b transitions,[7] and are observed at 11 590, 18 000, and 27 410 cm^{-1}, respectively. The sharp features observed at 12 530 and 13 090 cm^{-1} are due to the $^4A_2 \rightarrow {}^2E$ and $^2T_1$ transitions, respectively.[10] Also shown is the emission spectrum, which was reproduced from Ref. 9. It is obvious that the luminescence is the result of the inverse process represented by the nearby absorption band, and is therefore assignable to the $^4T_2 \rightarrow {}^4A_2$ transition.

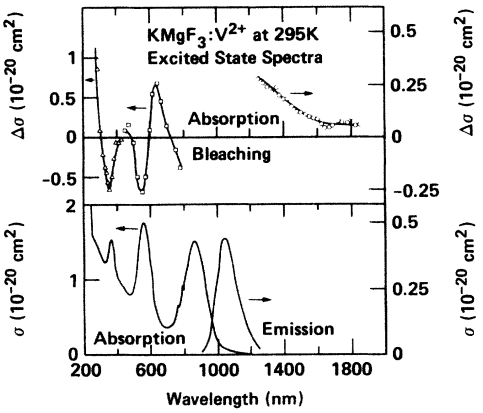

FIG. 2. Spectra of $KMgF_3:V^{2+}$ at room temperature in absolute units of cross section. The upper frame contains the difference spectra that result from optically pumping the V^{2+} ions; three different experimental arrangements were used to accumulate the data shown. In the lower frame, the conventional absorption and emission spectra are plotted.

In the upper frame of Fig. 2 the difference spectra that result from optically pumping V^{2+} to the $^4T_2$ excited state are shown. In the ultraviolet (uv) region, indicated by triangular data points, we observe the bleaching of the $^4A_2 \rightarrow {}^4T_1b$ absorption band at 365 nm, and a sharp ESA edge at energies greater than 36 500 cm^{-1} (272 cm). McClure and co-workers[11] have reported the existence of a strong band near 46 000 cm^{-1} for $KMgF_3:V^{2+}$. The same final state may be involved in the ESA edge. These workers have assigned this band to a $d \rightarrow s$ transition on the basis of numerous studies of divalent transition-metal ions in fluoride hosts. We were able to provide an absolute scale for these ESA measurements by assigning the $^4A_2 \rightarrow {}^4T_1b$ bleaching peak the same value for the cross section as the corresponding ground-state band. The data represented by triangles in Fig. 2 were also adjusted downward by about 1×10^{-20} cm^2 to compensate for what we believe was an electronically induced base-line shift. (No other data received such manipulation.)

We see from Fig. 2 that the data in the visible region appear as an "S"-shaped curve. This line shape can be explained as resulting from comparable contributions from the $^4T_2 \rightarrow {}^4T_1b$ ESA peak and the bleaching of the $^4A_2 \rightarrow {}^4T_1a$ absorption. If this were the case, it should be possible to add the appropriate amount of the ground-state spectrum to the difference curve in order to isolate the ESA band. This procedure is based on a somewhat subjective decision as to what appears to be a reasonable ESA line shape, since an independent means of accurately determining the excited-state population does not seem to exist. The result of this addition process is displayed in Fig. 3. Also shown is the spectrum acquired at 10 K, which appears to be somewhat narrower than the room-temperature result. By taking into account the known fraction of the ground-state spectrum that was added to the difference spectrum, it was possible to plot the absolute cross-section scales indicated for these data.

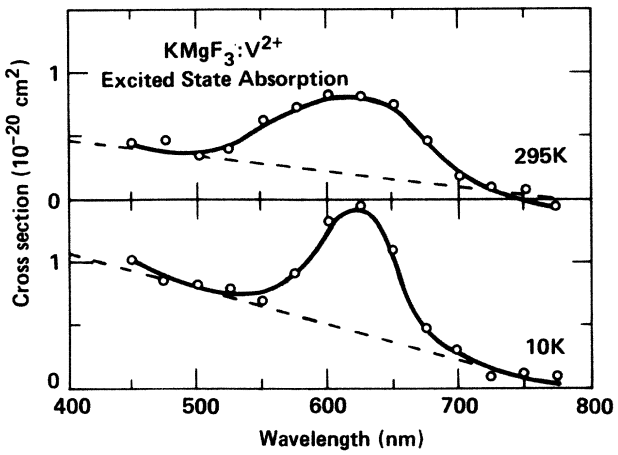

FIG. 3. Excited-state absorption spectra of $KMgF_3:V^{2+}$ as determined by adding the appropriate amount of the ground-state absorption spectrum to compensate for the bleaching observed in the difference spectra of Fig. 2.

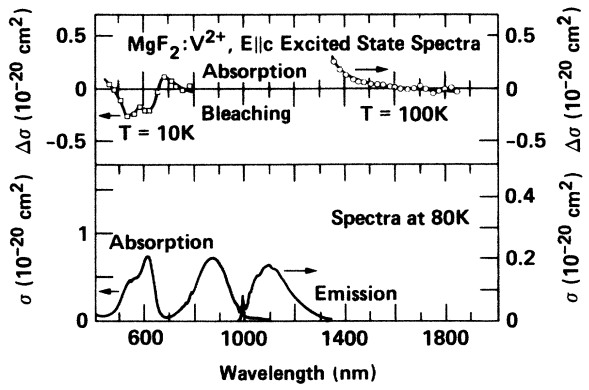

FIG. 4. E||c spectra of $MgF_2:V^{2+}$ obtained at the indicated temperatures. The excited-state absorption and the ground-state bleaching of the optically pumped spectra appear in the upper frame; the conventional absorption and emission spectra are in the lower frame.

In order to test whether this ESA band is due to the $^4T_2 \rightarrow {}^4T_1 b$ transition, we suggest that, in the absence of lattice relaxation, the energy of the transition depicted in Fig. 3 is predicted to occur at

$$E_{\text{calc}}({}^4T_2 \rightarrow {}^4T_1 b) = E({}^4A_2 \rightarrow {}^4T_1 b) - E({}^4A_2 \rightarrow {}^4T_2) \, . \tag{6}$$

By utilizing the data in the lower frame of Fig. 2 we calculate the transition to be near $27\,410\ \text{cm}^{-1} - 11\,590\ \text{cm}^{-1} = 15\,820\ \text{cm}^{-1}$, compared to the actual position of the band at $16\,000\ \text{cm}^{-1}$, as seen in Fig. 3. The close agreement provides strong support for this assignment of the ESA band. In addition the bandwidth is typical of the widths observed for the ground-state spectra. As discussed in Sec. I, this particular ESA band is expected to be broad since the $t_2^2 e \rightarrow t_2 e^2$ interconfigurational transition is involved.

Finally we refer now to the infrared ESA spectrum displayed in Fig. 2. This spectrum could not be scanned at wavelengths less than 1250 nm, since the emission from the sample became too intense compared to the probe beam source. It is clear, however, that the ESA band peaks at a wavelength < 1250 nm ($> 8000\ \text{cm}^{-1}$) and has a full width at half maximum of $> 2000\ \text{cm}^{-1}$. The only transition which can be responsible for this absorption is the $^4T_2 \rightarrow {}^4T_1 a$ transition. Using the same arguments, as discussed above, the predicted peak position of this band is given by

$$E({}^4T_2 \rightarrow {}^4T_1 a) = E({}^4A_2 \rightarrow {}^4T_1 a) - E({}^4A_2 \rightarrow {}^4T_2) \, . \tag{7}$$

Substituting in the appropriate values we get $18\,000\ \text{cm}^{-1} - 11\,590\ \text{cm}^{-1} = 6410\ \text{cm}^{-1}$, in substantial disagreement with the observed value of $> 8000\ \text{cm}^{-1}$. Furthermore, since both the $^4T_2$ and $^4T_1 a$ states are derived from the $t_2^2 e$ configuration, the transition should have been observed as a sharp feature. The general shape of this spectrum is, nonetheless, in agreement with the ESA results for the $^4T_2$ state of Cr^{3+} in $Gd_3Sc_2Ga_3O_{12}$, as obtained by Andrews *et al.*[12] These workers have indicated that they believe coupling to non-totally-symmetric distortions is the source of the striking disagreement between the simple predictions mentioned above and the actual experimental results; we will discuss this possibility in Sec. IV.

Referring to Fig. 2, we see that the cross section of the ESA band is quite similar to that of the emission band. We note in passing that the cross section of the infrared ESA curve was determined by comparison to the bleaching signal of the $^4A_2 \rightarrow {}^4T_2$ ground-state absorption band. Now, Moulton, Fahey, and Krupke have conducted a careful measurement of the stimulated emission cross section for $KMgF_3:V^{2+}$, and have found that $\sigma_{\text{meas}} = 0.16 \times 10^{-20}\ \text{cm}^2$.[4] On the other hand, the peak cross section is expected to be $\sigma_{\text{calc}} = 0.44 \times 10^{-20}\ \text{cm}^2$ on the basis of the emission line shape and lifetime. Moulton *et al.* have attributed the difference between the measured and calculated values of the cross section to the presence of ESA, viz.

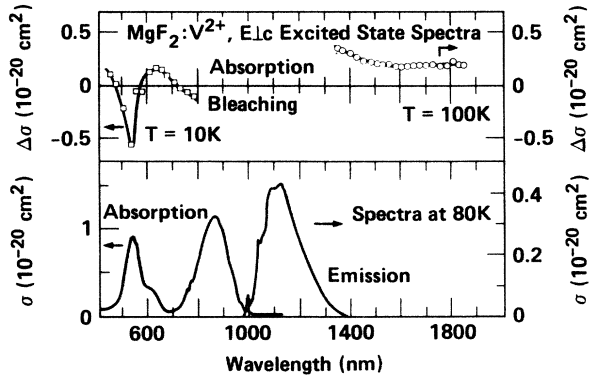

FIG. 5. E⊥c spectra of $MgF_2:V^{2+}$, presented in analogy to the data of Fig. 4.

$$\sigma_{ESA}=\sigma_{calc}-\sigma_{meas}\ . \tag{8}$$

We thus infer from the gain measurements that $\sigma_{ESA}=0.28\times10^{-20}$ cm^2. Although it is not completely clear how the infrared ESA curve of Fig. 2 should be extrapolated into the emission band region, inspection of the data reveals that the value of 0.28×10^{-20} cm^2 near 1064 nm is certainly within reason. It is very gratifying to find that the ESA data are essentially in agreement with the previously reported gain measurements.

B. $MgF_2:V^{2+}$

The MgF_2 crystal has the rutile lattice structure. Since MgF_2 is a uniaxial crystal, spectra with the electric vector of the light wave oriented both parallel and perpendicular to the C axis are required.[13] These results are shown in Figs. 4 and 5.

The $^4A_2\rightarrow{}^4T_2$ and ^4T_1a absorption bands are shown in the lower frames of Figs. 4 and 5; the absorption and emission data were reproduced from Ref. 14. By comparing the data in Figs. 4 and 5, it is seen that the two components of the $^4A_2\rightarrow{}^4T_1a$ band behave differently in polarized light. Sturge *et al.* have previously addressed in detail the nature of the nonoctahedral perturbations which induce the splitting.[7] Finally, the $^4T_2\rightarrow{}^4A_2$ emission spectra are also shown in these figures.

The excited-state difference spectra are plotted in the upper frames of Figs. 4 and 5. The bleaching of the $^4A_2\rightarrow{}^4T_1a$ band is observed for each of the polarizations and the double-peaked structure is clearly seen for the E||c polarization. As also occurred in the $KMgF_3:V^{2+}$ spectra, the ESA band is found to overlap the features due to bleaching. In Fig. 6, the appropriate amount of the ground-state absorption spectra has been added to the difference spectra, resulting in the pure $^4T_2\rightarrow{}^4T_1b$ ESA curves. The results for the two polarizations appear to be similar.

The infrared ESA spectra are in the upper frames of Figs. 4 and 5. As was the case for $KMgF_3:V^{2+}$ we can observe only the long-wavelength tail of the ESA feature due to the experimental interference resulting from the sample luminescence. A base-line shift of uncertain origin is observed for E⊥c. Moulton, Fahey, and Krupke found that the measured peak stimulated emission cross section of $MgF_2:V^{2+}$ was about 0.1×10^{-20} cm^2 for the E⊥c polarization, while the value was expected to be in the range of 0.4×10^{-20} cm^2.[3] The large discrepancy can be attributed to the effects of ESA in agreement with observation that the ESA and emission cross sections of Fig. 5 are of comparable magnitude. This is the same conclusion derived for $KMgF_3:V^{2+}$.

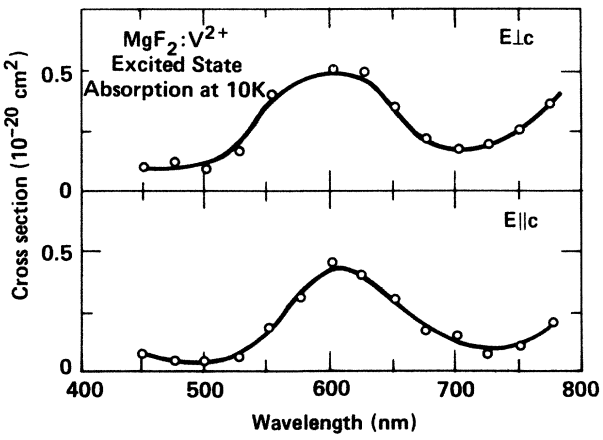

FIG. 6. E⊥c and E||c excited-state spectra of $MgF_2:V^{2+}$ at 10 K. The spectra were calculated by adding the appropriate amount of the ground-state absorption spectrum to the difference spectra in Figs. 4 and 5.

IV. DISCUSSION

The $^4T_2(t_2^2e)\rightarrow{}^4T_1a(t_2^2e)$ infrared ESA band has considerable technical and theoretical significance. From the technical viewpoint, this absorption seems to be the important loss mechanism of V^{2+} lasers. On the other hand, the experimental results for $KMgF_3$ appear to provide new insight into the influence of the Jahn-Teller effect (JTE) on optical transitions involving triply degenerate states. Since the a_{1g} distortion between the $^4T_2$ and $^4T_1$ a states is expected to be small, non-totally-symmetric (NTS) distortions must be considered as a possible source of the observed bandwidth and blue shift of the absorption. There is evidence from a previous ESA investigation for the relative importance of a_{1g} and NTS displacements in optical transitions of $3d^3$ ions. Fairbank *et al.*[15] measured ESA of Cr^{3+} in Al_2O_3, emerald, and MgO, where the crystal field is strong and the ^2E level is the initial state for ESA. They observed both narrow-line and broad-band spectra. Since the ESA spectrum from the ^2E state includes many more spin-allowed transitions than from the $^4T_2$, it is possible to gain from these results some insight into the effects of lattice relaxation in various types of excited states. In examining those spectra we found that for all those transitions to states with configurations *differing* from that of the $^2E(t_2^3)$ state, such as t_2^2e and t_2e^2, the narrow lines (small Huang-Rhys factors) occur when the terminal level is an orbital singlet, and the broad bands occur for orbital doublets (^2E) and triplets ($^2T_1$ and $^2T_2$). The a_{1g} coupling is expected to affect all of these states more or less equally if they involve the same change in strong-field configuration, i.e., $t_2^3\rightarrow t_2^2e$, etc. On the other hand, only orbitally degenerate states are affected to first order by NTS displacements. Therefore, we argue that the results of Fairbank *et al.*[15] imply that the effects of NTS displacements are considerably larger than a_{1g} displacements, even when the configuration change $t_2^3\rightarrow t_2^2e$ is involved.

In the present work, no change in configuration is involved in the $^4T_2(t_2^2e)\rightarrow{}^4T_1a(t_2^2e)$ transition, and it seems reasonable to neglect completely the cubic a_{1g} coordinate in a first-order analysis. The NTS coupling for an orbitally degenerate state in perfect cubic symmetry results in Jahn-Teller distortion. When the local field departs from cubic symmetry, however, as in MgF_2, the

effects of lattice relaxation are more complex and variable. In what follows, we will briefly outline the general formulation of the JTE for a T state.[16] We will apply these results to the $^4T_2$ and ^4T_1a states of V^{2+} in $KMgF_3$ and then to the ^4T_1b state. Finally, the effects of a static distortion from octahedral symmetry will be discussed in connection with the ESA spectra of V^{2+} in MgF_2.

The e_g-type distortions are typically expected to interact more strongly with the electronic states of an octahedrally coordinated transition-metal ion, than those distortions having t_{2g} symmetry. This is true because the e_g normal coordinate results in direct changes of the metal-anion bond lengths, while the t_{2g} distortion primarily affects the bond angles of the cluster, and therefore will not modify the V^{2+} electronic structure as significantly. The two partners of the e_g distortion are designated as θ and ε, transforming as $2z^2$-x^2-y^2 and x^2-y^2, respectively, as depicted in Fig. 7(a). The potential in the e_g coordinate can be written as[16]

$$V_e=\left[\frac{\partial V_e}{\partial Q_\theta}\right]Q_\theta+\left[\frac{\partial V_e}{\partial Q_\varepsilon}\right]Q_\varepsilon+\tfrac{1}{2}k_e(Q_\theta^2+Q_\varepsilon^2)\,, \tag{9}$$

where the linear terms have been introduced to account for the JTE, and the quadratic term gives rise to the usual harmonic potential. At this point, we need to calculate the matrix elements of Eq. (9) for the T state basis functions. In fact, it is well known that if the state vector transforms as ($\alpha=X$, $\beta=y$, $\gamma=Z$) or ($\xi=yz$, $\eta=xz$, $\zeta=xy$) for a T_1 or T_2 state, respectively, the e_g vibrational Hamiltonian can be diagonalized to give[16]

$$H_e=A\begin{bmatrix}-\frac{1}{2}Q_\theta+\frac{\sqrt{3}}{2}Q_\varepsilon & 0 & 0\\ 0 & -\frac{1}{2}Q_\theta-\frac{\sqrt{3}}{2}Q_\varepsilon & 0\\ 0 & 0 & Q_\theta\end{bmatrix}$$
$$+T_e+\tfrac{1}{2}k_e(Q_\theta^2+Q_\varepsilon^2)\,, \tag{10}$$

where T_e is the kinetic energy operator and A is a constant that depends on the nature of the electronic state. Inspection of the linear combinations of Q_θ and Q_ε in the diagonal matrix elements reveals that, from left to right, they transform as $2x^2$-y^2-z^2, $2y^2$-x^2-z^2, and $2z^2$-x^2-y^2. Equation (10) therefore indicates that the JTE results in three equivalent paraboloids in e_g space, whose (Q_ε,Q_θ) minima occur at $(-\sqrt{3}A/2k_e, A/2k_e)$, $(\sqrt{3}A/2k_e, A/2k_e)$, and $(0,-A/k_e)$. Because the matrix is diagonalized, the three paraboloids are noninteracting, or "disjointed," and can be treated as three independent potential surfaces.

Next, we consider the actual wave functions of the $^4T_2$ or ^4T_1a electronic states:[8]

$$|T_1\alpha\rangle=\tfrac{1}{2}|t_2\eta\rangle|t_2\zeta\rangle(-|e\theta\rangle+\sqrt{3}|e\varepsilon\rangle)\,, \tag{11a}$$
$$|T_1\beta\rangle=\tfrac{1}{2}|t_2\xi\rangle|t_2\zeta\rangle(-|e\theta\rangle-\sqrt{3}|e\varepsilon\rangle)\,, \tag{11b}$$
$$|T_1\gamma\rangle=|t_2\xi\rangle|t_2\eta\rangle|e\theta\rangle\,, \tag{11c}$$
$$|T_2\xi\rangle=\tfrac{1}{2}|t_2\eta\rangle|t_2\zeta\rangle(\sqrt{3}|e\theta+|e\varepsilon\rangle)\,, \tag{11d}$$
$$|T_2\eta\rangle=\tfrac{1}{2}|t_2\zeta\rangle|t_2\xi\rangle(-\sqrt{3}|e\theta\rangle+|e\varepsilon\rangle)\,, \tag{11e}$$
$$|T_1\zeta\rangle=-|t_2\xi\rangle|t_2\eta\rangle|e\varepsilon\rangle\,. \tag{11f}$$

Since the spin multiplicity is maximal, all the spins are aligned for the states of interest here. The spin parts of the wave functions therefore have no effect on our calculations and have been omitted from Eqs. (11).

Now, it has often been asserted that the t_2 orbitals are nearly nonbonding in nature, while the e orbitals are mostly responsible for the transition-metal ion-anion interactions with the octahedral environment.[17] If we assume this to be the case, we can use the wave functions of Eqs. (11) and the potential of Eq. (9) to calculate the values of A in Eq. (10) for the $^4T_2$ and ^4T_1a states to be[18]

$$A(^4T_2)=-\frac{1}{\sqrt{2}}\langle e\|\partial V_e/\partial Q\|e\rangle\,, \tag{12a}$$
$$A(^4T_1a)=\frac{1}{\sqrt{2}}\langle e\|\partial V_e/\partial Q\|e\rangle\,, \tag{12b}$$

where the right-hand sides are expressed in terms of reduced matrix elements. In other words, $A(^4T_2)=-A(^4T_1a)$, and the two states have their vibrational potential minima at opposite signs of the e_g distortion. Physically, this can be seen to be the result of the fact

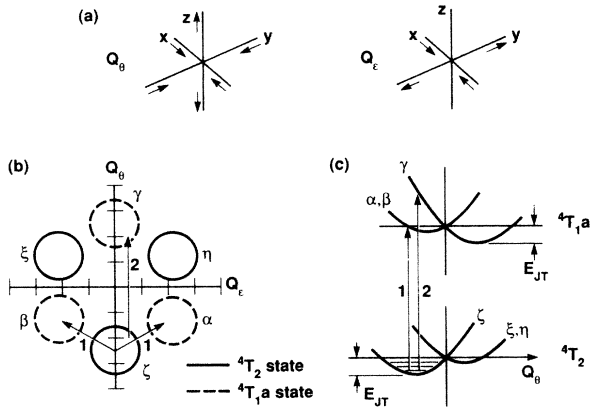

FIG. 7. Two-dimensional schematic representation of contours of the vibrational potential-energy surfaces of the $^4T_2$ and ^4T_1a states of the V^{2+} impurity. The Jahn-Teller effect produces three disjointed paraboloids in the e_g coordinate space. The e_g partners are illustrated in (a). The two types of $^4T_2\rightarrow{}^4T_1a$ transitions possible are indicated schematically by the arrows in (b); the actual transitions occur perpendicular to the plane of the figure with no change of (Q_ε,Q_θ) coordinates. Note that electron-electron repulsion effects actually lead to a $\sim$6400-cm^{-1} vertical separation between the $^4T_2$ and ^4T_1a states. Equations (13)–(15) describe the peak position, bandwidth, and relative intensity of these two transitions. In frame (c), the cross section of the vibrational potential surfaces of (b) along the Q_θ axis at $Q_\varepsilon=0$ is shown. The two possible $^4T_2\rightarrow{}^4T_1a$ ESA transitions are indicated.

that the wave functions of the $^4T_2$ and ^4T_1a states in Eqs. (11) differ by the interchange of the $|e\theta\rangle$ and $|e\varepsilon\rangle$ orbitals. For example, the $|T_2\zeta\rangle$ state will be shifted down in energy by a $-Q_\theta$ distortion since the $|e\varepsilon\rangle$ orbital in that state has lobes pointing toward the fluorines along the x and y axes. The $|T_1\gamma\rangle$ state, on the other hand, is raised in energy by that $-Q_\theta$ distortion since the $|e\theta\rangle$ orbital points toward the fluorines along the z axis. The potential-energy paraboloids of the $^4T_2$ and ^4T_1a states are represented in the two-dimensional (Q_ε,Q_θ) plane as six circular contours, as shown in Fig. 7(b). ESA transitions in the Franck-Condon approximation occur from an occupied vibrational well of the $^4T_2$ state to a point on one of the ^4T_1a wells at the *same* coordinate (Q_ε,Q_θ). The two types of $^4T_2\rightarrow{}^4T_1a$ transitions that are expected to occur are represented by arrows in Fig. 7(b). A cross section of the potential surfaces of Fig. 7(b) along the Q_θ axis is shown in Fig. 7(c). The vertical arrows identify the ESA transitions, Nos. 1 and 2, for an ion that is initially in the ζ partner of the $^4T_2$ state. It is apparent that transition No. 2 samples a point on the ^4T_1a potential surface that is at a greater energy and has a steeper slope than transition No. 1. In fact, we find that these two transition energies are calculated to be at

$$E_1=\Delta E+E_{\rm JT}\ , \tag{13a}$$

$$E_2=\Delta E+4E_{\rm JT}\ , \tag{13b}$$

where the JT energy $E_{\rm JT}=A^2/2k_e$, and ΔE is the separation of the $^4T_2$ and ^4T_1a states in the absence of the JTE (due mostly to the difference in the electron-electron repulsion parameters). The transitions indicated by the shorter and longer arrows of Fig. 7 are described by Eqs. 13(a) and 13(b), respectively. The full width at half maximum (FWHM) of the bands at high temperature are[9]

$$\Delta_1=(16\ln 2)^{1/2}(E_{\rm JT}kT)^{1/2}\ , \tag{14a}$$

$$\Delta_2=(64\ln 2)^{1/2}(E_{\rm JT}kT)^{1/2}\ . \tag{14b}$$

Lastly, the relative transition strength of the two bands is

$$\frac{W_2}{W_1}=\frac{|\langle e\|P\|e\rangle|^2}{1.5\,|\langle t_2\|P\|t_2\rangle|^2}\ , \tag{15}$$

where the operator P serves the dual function of inducing the nominally forbidden $d\rightarrow d$ transitions by the light field and also by the appropriate odd-parity-vibrational interactions.

We recall from Sec. III that, on the basis of the a_{1g} distortions only, the $^4T_2\rightarrow{}^4T_1a$ spectrum is predicted to be observed as a sharp line at 6400 $\rm cm^{-1}$ (1560 nm). If we take the actual band peak to be at 8000 $\rm cm^{-1}$ (the shortest wavelength reported for the infrared ESA data in Fig. 2), and we assume that $\Delta E=6400\ \rm cm^{-1}$, the ESA feature can be explained as arising solely from the transition represented by Eq. 13(b), or the larger arrows of Fig. 7. Using Eq. 13(b), we obtain $E_{\rm JT}>400\ \rm cm^{-1}$, and substituting this value into Eq. 14(b), we find $\Delta_2>1900\ \rm cm^{-1}$, in agreement with the observed FWHM of $>2000\ \rm cm^{-1}$.

On the basis of Eqs. (13) and (14), we would expect to observe another band at 6800 $\rm cm^{-1}$ (1470 nm) having a width of about 1000 $\rm cm^{-1}$. Such a transition is not easily discerned from the noisy data in Fig. 2. The question of its relative intensity, however, must be considered. Through inspection of Eq. (15), we see that the transition described by Eqs. 13(b) and 14(b) is due to an $e\rightarrow e$ electronic transition, while that of Eqs. 13(a) and 14(a) arises from a $t_2\rightarrow t_2$ transition. It is possible that the e electrons interact more strongly with the odd-parity vibrations and therefore the $e\rightarrow e$ transition may turn out to be significantly more allowed than the $t_2\rightarrow t_2$ transition. While we do not have independent confirmation of this suggestion, the infrared ESA data of Fig. 2 can be explained by assuming that $E_{\rm JT}>400\ \rm cm^{-1}$, and that only the $e\rightarrow e$ transition is strong enough to be observed.

We digress at this point to consider what is currently known about the JT effect for the V^{2+} impurity. All of the JT analyses of the $KMgF_3{:}V^{2+}$ system have thus far been based on considering the energetic separations of the four spin-orbit (SO) components of the $^4T_2$ state. The main experimental observation is that the SO splittings are much less than what is expected from the free-ion value of the SO coupling constant. This reduction has been attributed to the quenching of the orbital angular momentum (known as the Ham effect).[20] Using this method, the value of $E_{\rm JT}$ was determined to be on the order of 200 $\rm cm^{-1}$ for $KMgF_3{:}V^{2+}$.[21–23]

We therefore encounter the question as to why the Ham effect predicts that $E_{\rm JT}$ is about 200 $\rm cm^{-1}$, while the present analysis places its value closer to 400 $\rm cm^{-1}$. The reason for this discrepancy is probably due to the approximate nature of both analyses, and the fact that they sample differently the potential-energy surfaces that are involved. Referring to Figs. 7(b) and 7(c), we note that the Ham effect depends sensitively on the vibrational overlap of the lower vibrational states of the three displaced paraboloids of the $^4T_2$ states. This overlap involves primarily the behavior of the ground vibrational wave functions far from the potential minima. The present analysis, however, depends on the transition between low-lying $^4T_2$ vibrational states and more highly excited ^4T_1a vibrational states, and therefore is more directly related to the general topology of the ^4T_1a surfaces. Some previous investigations do indeed seem to support the idea of larger values of $E_{\rm JT}$ than those obtained from spin-orbit splittings. Since the e electron of the t_2^2e configuration is expected to provide most of the coupling to e_g vibrations, we may infer typical values of $E_{\rm JT}$ from studies on the $3d^9$ configuration of Cu^{2+} in octahedral fluorine coordination. The Cu^{2+} ground state has a single e hole and its first excited state has a t hole. An observed absorption band at $\sim$8000 $\rm cm^{-1}$ in K_2CuF_4 can be assigned to transitions between Jahn-Teller-split states of the ^2E orbital doublet state resulting from the e hole.[24] Neglecting anharmonicity, this would correspond to $E_{\rm JT}\sim 2000\ \rm cm^{-1}$. For comparison, a recent *ab initio* calculation yielded $E_{\rm JT}\sim 1000\ \rm cm^{-1}$.[25]

We would expect E_{JT} for the $^4T_2(t_2^2e)$ and $^4T_1a(t_2^2e)$ states in sixfold fluorine coordination not to differ greatly from these results. It is therefore conceivable that the $^4T_2 \rightarrow {}^4T_1a$ ESA bands of Figs. 2, 4, and 5 might be even broader than we have estimated here. In view of this possibility, it is important to develop an experimental approach to measuring the ESA spectrum at shorter wavelengths where it overlaps the emission band.

We found in Sec. III that the $^4T_2 \rightarrow {}^4T_1b$ transition was close to the peak position predicted from the ground-state absorption spectra. This can be understood by considering the wave functions (to an arbitrary phase factor) for the $^4T_1b(t_2e^2)$ state:

$$|{}^4T_1b\alpha\rangle = |e\theta\rangle\,|e\varepsilon\rangle\,|t_2\xi\rangle\,, \tag{16a}$$

$$|{}^4T_1b\beta\rangle = |e\theta\rangle\,|e\varepsilon\rangle\,|t_2\eta\rangle\,, \tag{16b}$$

$$|{}^4T_1b\gamma\rangle = |e\theta\rangle\,|e\varepsilon\rangle\,|t_2\zeta\rangle\,. \tag{16c}$$

Using these wave functions and the form of the Jahn-Teller terms in Eq. (9), we find that the value of A in Eq. (10) is zero. Thus, the driving force for the Jahn-Teller distortion is absent in this state because the e electrons form a symmetrically occupied half-filled shell. The $^4T_2 \rightarrow {}^4T_1b$ transition, is therefore, anticipated to be observed as a single band displaced by only E_{JT} (rather than $4E_{JT}$ as for the $^4T_2 \rightarrow {}^4T_1a$ transition) due to the e_g coupling alone. The additional fact that much of the bandwidth is caused by the a_{1g} displacement makes the influence of the JTE inconsequential in this case.

In MgF_2, each V^{2+} ion is in a site of orthorhombic symmetry, which may be approximated as a linear combination of tetragonal and trigonal deformations of the fluorine octahedron at the V^{2+} site. This low-symmetry crystal field lifts the degeneracy of the $^4T_2$ and ^4T_1a states, thus precluding, or greatly modifying,[7] any Jahn-Teller distortion. The coupling to e_g distortions continues, however, to cause relaxation of the neighboring ions in these states, although the adiabatic potential-energy surfaces are expected to be much more complex than those shown in Fig. 7. It is also apparent from the different wave functions of the $^4T_2$ and ^4T_1a states that the effects of particular excited-state relaxation modes on those states will differ, thus leading to broadening and shifting of the $^4T_2 \rightarrow {}^4T_1a$ ESA band. This is illustrated schematically in Fig. 8 for a simpler case of a V^{2+} or Cr^{3+} ion in a tetragonal site, in which either a $+Q_\theta$ or a $-Q_\theta$ distortion is imposed by the crystal structure. These distortions split each orbital triplet into orbital doublet and singlet states. Because of the interchange of the $|e\theta\rangle$ and $|e\varepsilon\rangle$ orbitals in the ^4T_1a and $^4T_2$ wave functions in Eqs. (11), the order of the singlet and doublet components is reversed for these states, as is shown in Fig. 8.

For large static tetragonal fields, $(Q_\theta)_0$, lattice relaxation in the metastable $^4T_2$ state will be predominantly of the same sign as $(Q_\theta)_0$, since the lowest (singlet or doublet) components are eigenstates of $(Q_\theta)_0$. The energies of the orbital components at the "relaxed" configuration of the $^4T_2$ state are indicated schematically by dashed lines in Fig. 8. Note that, for either sign of the tetragonal distortion, the ESA will be broadened by relaxation and *also* by the splitting caused by the static field. The effects of such a static field on laser efficiency appear to be most pronounced for $(Q_\theta)_0 < 0$ (an "oblate" octahedron), because the shift to higher energy (toward the $^4T_2 \rightarrow {}^4A_2$ emission peak) is most pronounced in that case.

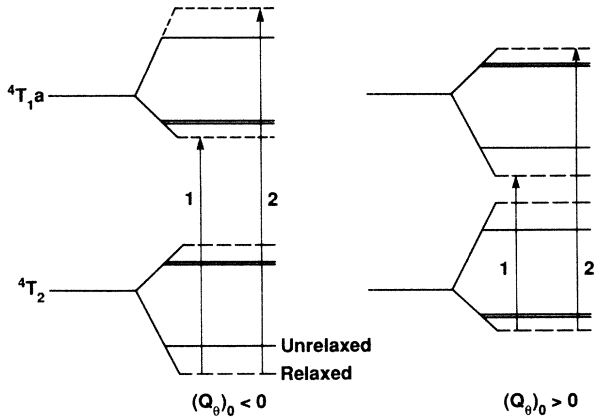

FIG. 8. Schematic representation of ESA for a V^{2+} or Cr^{3+} ion in a static, tetragonal field $(Q_\theta)_0$ of either sign. Solid lines are static splittings at the ground-state nearest-neighbor positions. Dashed lines locate relaxed electronic states for an occupied $^4T_2$ state.

The static splitting of the ^4T_1a state will lead to two ESA bands originating from the relaxed $^4T_2$ level. If we associate the shoulder on the long-wavelength side of the emission band in Figs. 4 and 5 with transition 2 in Fig. 8, then the "baseline shift" at long wavelengths in the E⊥c ESA data in Fig. 5 could result from transition 1 in Fig. 8. ESA data at longer wavelengths would be helpful in investigating this possibility.

V. CONCLUSION

We have obtained the excited-state absorption (ESA) spectra for V^{2+} in $KMgF_3$ and for the two polarizations of the MgF_2 host. We concentrated our theoretical analysis on the $KMgF_3$:V^{2+} system since the Mg^{2+} site is known to be rigorously octahedral thereby simplifying the spectra and their interpretation. The ESA spectra contained features related to the $^4T_2(t_2^2e) \rightarrow {}^4T_1a(t_2^2e)$ and $^4T_2(t_2^2e) \rightarrow {}^4T_1b(t_2e^2)$ d-d transitions, as well as the edge of the $d \rightarrow s$ transition in the ultraviolet region. The properties of the $^4T_2 \rightarrow {}^4T_1b$ transition are found to be determined mostly by the a_{1g}-type displacement between the two states. On the other hand, the $^4T_2 \rightarrow {}^4T_1a$ transition is found to be dramatically influenced by the $T \otimes e_g$ Jahn-Teller effect. The spectral evidence of the e_g distortion is the observation of a very broad feature, in striking contrast to the sharp line that is predicted solely

on the basis of the a_{1g} mode. This $^4T_2 \rightarrow {}^4T_1 a$ band is observed to seriously overlap the emission spectrum, resulting in a large reduction of the effective stimulated emission cross section. The ESA provides a good explanation as to why the efficiencies of V^{2+} lasers have previously been found to be quite low.

Note added in proof. It has come to our attention that R. Moncorge and T. Benyattou at the Université de Lyon, France, have simultaneously performed similar measurements of the excited-state absorption for V^{2+} in MgF_2 and $KMgF_3$. Our results appear to be similar.

ACKNOWLEDGMENTS

We are indebted to Gary Ullery for maintaining the flashlamp-pumped dye laser during the course of this work, and to Dr. William F. Krupke, for his comments and encouragement.

[1]L. F. Johnson, H. J. Guggenheim, and R. A. Thomas, Phys. Rev. **149**, 179 (1966).

[2]W. F. Krupke, in *Proceeding of the International Conference on Lasers 1980,* edited by C. B. Collins (STS, McLean, VA, 1980).

[3]P. F. Moulton, R. E. Fahey, and W. F. Krupke, in *1981 Laser Program Annual Report, Lawrence Livermore National Laboratory,* edited by E. V. George (National Technical Information Service, Springfield, VA, 1982), pp. 7–94.

[4]P. F. Moulton, R. E. Fahey, and W. F. Krupke, in *1982 Laser Program Annual Report, Lawrence Livermore National Laboratory,* edited by C. D. Hendricks (National Technical Information Service, Springfield, VA, 1983), pp. 6–91.

[5]U. Brauch and U. Dürr, Opt. Commun. **55**, 35 (1985).

[6]W. Knierim, A. Honold, U. Brauch, and U. Dürr, J. Opt. Soc. Am. **B3**, 119 (1986).

[7]M. D. Sturge, F. R. Merritt, L. F. Johnson, H. J. Guggenheim, and J. P. van der Ziel, J. Chem. Phys. **54**, 405 (1971).

[8]S. Sugano, Y. Tanabe, and H. Kamimura, *Multiplets of Transition-Metal Ions in Crystals* (Academic, New York, 1970).

[9]P. F. Moulton, R. E. Fahey, and W. F. Krupke in *Laser Program Annual Report 83, Lawrence Livermore National Laboratory,* edited by C. D. Hendricks (National Technical Information Service, Springfield, VA, 1984), pp. 7–78.

[10]M. D. Sturge and H. J. Guggenheim, Phys. Rev. B **2**, 2459 (1970).

[11]J. F. Sabatini, A. E. Salwin, and D. S. McClure, Phys. Rev. B **11**, 3832 (1975).

[12]L. J. Andrews, S. M. Hitelman, M. Kokta, and D. Gabbe, J. Chem. Phys. **84**, 5229 (1986).

[13]M. D. Sturge, Solid State Commun. **9**, 899 (1971).

[14]Peter Moulton (unpublished).

[15]W. M. Fairbank, Jr., G. K. Klauminzer, and A. L. Schawlow, Phys. Rev. B **11**, 60 (1975).

[16]M. D. Sturge, in *Solid State Physics,* edited by F. Seitz, D. Turnbull, and H. Ehrenreich (Academic, New York, 1967), Vol. 20.

[17]C. J. Ballhausen, *Introduction to Ligand Field Theory* (McGraw-Hill, New York, 1962).

[18]J. S. Griffith, *The Theory of Transition-Metal Ions* (Cambridge University Press, Cambridge, England, 1971).

[19]A. M. Stoneham, *Theory of Defects in Solids* (Clarendon, Oxford, 1975).

[20]F. S. Ham, Phys. Rev. **138**, A1727 (1965).

[21]M. D. Sturge, Phys. Rev. B **1**, 1005 (1970).

[22]A. Ranfagni and G. Viliani, Phys. Status Solidi B **84**, 393 (1977).

[23]S. Muramatsu and N. Sakamoto, J. Phys. Soc. Jpn. **46**, 1273 (1979).

[24]R. Laiho, Phys. Status Solidi B **69**, 579 (1975).

[25]Sergei Yu. Shashkin and William A. Goddard III, Phys. Rev. B **33**, 1353 (1986).